

X1908+075: A PULSAR ORBITING IN THE STELLAR WIND OF A MASSIVE COMPANION

A. M. LEVINE¹, S. RAPPAPORT¹, R. REMILLARD¹, & A. SAVCHEVA¹

Draft version July 3, 2018

ABSTRACT

We have observed the persistent but optically unidentified X-ray source X1908+075 with the PCA and HEXTE instruments on *RXTE*. The binary nature of this source was established by Wen, Remillard, & Bradt (2000) who found a 4.4-day orbital period in results from the *RXTE* ASM. We report the discovery of 605 s pulsations in the X-ray flux. The Doppler delay curve is measured and provides a mass function of $6.1 M_{\odot}$ which is a lower limit to the mass of the binary companion of the neutron star. The degree of attenuation of the low-energy end of the spectrum is found to be a strong function of orbital phase. A simple model of absorption in a stellar wind from the companion star fits the orbital phase dependence reasonably well and limits the orbital inclination angle to the range $38^{\circ} - 72^{\circ}$. These measured parameters lead to an orbital separation of $\sim 60 - 80$ lt-s, a mass for the companion star in the range $9-31 M_{\odot}$, and an upper limit to the size of the companion of $\sim 22 R_{\odot}$. From our analysis we also infer a wind mass loss rate from the companion star of $\gtrsim 1.3 \times 10^{-6} M_{\odot} \text{ yr}^{-1}$ and, when the properties of the companion star and the effects of photoionization are considered, likely $\gtrsim 4 \times 10^{-6} M_{\odot} \text{ yr}^{-1}$. Such a high rate is inconsistent with the allowed masses and radii that we find for a main sequence or modestly evolved star unless the mass loss rate is enhanced in the binary system relative to that of an isolated star. We discuss the possibility that the companion might be a Wolf-Rayet star that could evolve to become a black hole in 10^4 to 10^5 yr. If so, this would be the first identified progenitor of a neutron star–black hole binary.

Subject headings: X-rays: binaries — pulsars: general — pulsars: individual (X1908+075) — stars: evolution — stars: winds, outflows

1. INTRODUCTION

X1908+075 is an optically unidentified, highly absorbed, and relatively faint X-ray source that appeared in surveys carried out with instruments on the *Uhuru*, *OSO 7*, *Ariel 5*, *HEAO-1*, and *EXOSAT* satellites. The early detections and position determinations are summarized by Wen, Remillard, & Bradt (2000, hereafter WRB). They conclude that the position of X1908+075 is likely to be within the overlapping region of the error box of a source detected in an *Einstein* IPC image and one of an array of *HEAO 1* A-3 position “diamonds”, and is thus known with an accuracy of $\sim 1'$. Inspection of the POSS plates within the source error box reveals no optical counterpart down to magnitude 20. This is consistent with the heavy optical extinction implied by the interstellar hydrogen column density of $\sim 4 \times 10^{22}$ atoms cm^{-2} measured on the basis of the low-energy absorption in the X-ray spectrum (see Shull & van Steenberg 1985).

The intensity of X1908+075 has been monitored for the past eight years using the All-Sky Monitor (ASM) aboard the *Rossi X-Ray Timing Explorer* (*RXTE*), and has typically been in the range 2-12 mCrab in the 2-12 keV energy band. WRB analyzed data from the first three years of operation of the ASM, and thereby discovered a 4.4 day periodicity in the X-ray intensity. The periodic component of the intensity variations is clearly energy dependent in both strength and detailed form. At most orbital phases, the variation is roughly sinusoidal while a relatively sharp dip forms the minimum in the 5-12 keV band. These characteristics suggest that the

modulation is produced by a varying amount of absorption along the line of sight as the source moves through the stellar wind of a massive companion star. The hard X-ray spectrum led WRB to also suggest that this source could be an X-ray pulsar.

The possibility that X1908+075 might be an X-ray pulsar led us to carry out a set of pointed observations with the PCA and HEXTE instruments on *RXTE* in late 2000 and early 2001. The data revealed the presence of strong X-ray pulsations at a period of 605 seconds. We were also able to detect Doppler delays in the pulse arrival times. However, because the number of independent high-quality pulse arrival times obtained from this data set was small, it proved difficult to unambiguously disentangle orbital effects from intrinsic changes in the pulse period. The latter could, in principle, be quite large for a neutron star rotating with a period as long as 600 s (see, e.g., Bildsten et al. 1997; Delgado-Martí et al. 2001). Therefore, we obtained additional observations of the source with *RXTE* during late 2002 and early 2003.

In this paper we report the results of our analysis of the *RXTE* observations of X1908+075. The pointed observations are described in §2. A pulse timing analysis is described in §3. We present an accurate pulse period and a determination of the spin-down of the neutron star due to accretion and magnetic torques. The orbital Doppler delay curve is measured, thereby confirming the 4.4-day period found in the ASM X-ray light curve. The resultant mass function is $6.1 M_{\odot}$, indicating that the pulsar does indeed orbit a massive companion star. The results of an orbital-phase-dependent spectral analysis are presented in §4. We detect a very pronounced modulation of the low energy attenuation as a function of orbital phase. In §5 we model this modulation by absorption in

¹ Department of Physics and Center for Space Research, MIT 37-575, 77 Massachusetts Ave, Cambridge, MA 02139; am1@space.mit.edu

a spherically symmetric stellar wind, whereby we obtain constraints on the orbital inclination, on the properties of the companion star, and on the stellar wind. We discuss the implications of our results in §6, including the possibility that this system may be the progenitor of a neutron star–black hole binary.

2. OBSERVATIONS

Pointed observations of X1908+075 were made with the Proportional Counter Array (PCA) and High-Energy X-ray Timing Experiment (HEXTE) on *RXTE*. The PCA consists of 5 Proportional Counter Units (PCUs) that are sensitive to X-ray photons in the range 2.5–60 keV. Each PCU has a collecting area of $\sim 1400 \text{ cm}^2$ and a collimator to limit the field of view to 1° in radius (Jahoda et al. 1996). Some of the PCUs are operated with reduced duty cycle in order to avoid problems associated with constant use. Only PCUs 0 and 2 were used in every observation. Data from the PCA observations were telemetered to the ground in the “GoodXenon” mode, which includes information on each good event with $1 \mu\text{s}$ time resolution and the instrument’s full energy resolution (255 channels). The HEXTE comprises two clusters, each of which includes 4 NaI scintillation detectors sensitive to photons in the range 15–250 keV that provide a total collecting area of 800 cm^2 per cluster. The detectors in each cluster view a common 1° radius field (Rothschild et al. 1998).

Between 2000 November 19 and 2001 February 22, we obtained 15 short observations with a typical exposure time in each of $\sim 2000 \text{ s}$. A total exposure of 35 ks was obtained in these observations, which we refer to collectively as “epoch 1”. Over all of the 15 observations there were, on average, 3.0 PCUs in operation. Eight of the observations were made during one orbital cycle of X1908+075 (~ 4 days), while the remaining 7 were performed nearly 3 months later. Fourier transforms of these data clearly exhibited the presence of X-ray pulsations with a period of 605 s.

Additional observations with the PCA and HEXTE were carried out on 39 occasions from 2002 December 23 through 2003 January 5 and on 32 occasions from 2003 January 30 through 2003 February 8 (“epoch 2”; 196 ks total exposure). On average, 3.5 PCUs were in operation. Each of these 71 observations in epoch 2 typically yielded $\sim 3000 \text{ s}$ of net exposure most often in the form of two contiguous time intervals separated by a $\sim 2000 \text{ s}$ gap due to Earth occultation of the target. Raw counting rate data from two of these 71 pointed observations are shown in Fig. 1 to illustrate the typical appearance of the X-ray pulsations and accompanying source variability. The X-ray intensity, in addition to exhibiting obvious pulsations, is also quite variable on timescales comparable to the pulse period and longer.

For pulsar timing purposes we used events with energies in the range 3.7–17 keV (channels 3–40) from both left and right sections of layer 1 of all operating PCUs. Event times were reduced to the Solar System barycenter. The average 3.7–17 keV background count rate in individual observations done in 2003–2003 ranges from 7.3 to $7.8 \text{ cts s}^{-1} \text{ PCU}^{-1}$. Background was not subtracted in our timing analyses.

To determine an appropriate model for spectral analyses, we used data from both the PCA and HEXTE.

In the PCA analyses we utilize 2.9–25 keV pulse height range data from all layers of PCU 2 only because that PCU was operational for all of the observations and because its calibration is superior, as judged by the analysis of contemporaneous PCA observations of the Crab Nebula. Spectral extractions and background subtractions for both the PCA and HEXTE were performed using the “FTOOLS” package, and spectral models were applied using “XSPEC”. Both of these software packages were provided by NASA/HEASARC.

3. PULSE TIMING AND ORBITAL ANALYSIS

A first estimate of the mean pulse period was obtained by binning the data from all of the epoch 2 (2002–2003) observations in 16-s bins and carrying out an FFT analysis of the resultant data train (2^{18} points). The FFT revealed a highly significant signal at a period of 604.76 s, as well as 5 very prominent higher harmonics of the fundamental. Also evident in the Fourier transform were a number of sidebands of the pulsations that were spaced in frequency by multiples of $1/4.4 \text{ days}^{-1}$. These sidebands were identified as due to the orbital motion of the neutron star about its companion. From the fundamental and the prominent harmonics and sidebands, we derived an average pulse period during these observations of 604.689 s.

We proceeded to fold the data from each of the 71 pointed observations from 2002–2003 modulo this value of the average pulse period. To form a “pulse template”, the individual pulse profiles were manually aligned to correct for small phase drifts and then averaged (see Fig. 2).

We then computed the cross correlation function (CCF) between the template and the folded profile from each of the individual observations. The phase difference for which the CCF reaches a maximum value is the best estimate of the pulsar phase relative to the folding ephemeris. Pulse arrival time delays are then simply obtained as the products of the phase differences and the folding period. Pulse arrival times were then computed by adding each time delay to the time of phase zero of a pulse near the middle of the observation interval. This analysis yielded a total of 69 pulse arrival times after we eliminated the results from 2 of the 71 observations for which the CCFs were possibly ambiguous. The pulse arrival time delays are listed in Table 1 and plotted in Figure 3. The Doppler delays due to the orbital motion are quite apparent in Figure 3, as is an overall quadratic behavior due to the slowdown in the rotation rate of the neutron star.

We fit the pulse arrival times with a 7-parameter model of the orbit and pulse period behavior. The arrival time of the n th pulse is given by

$$t_n = t_0 + nP + \frac{1}{2}n^2P\dot{P} + \frac{1}{c}a_x \sin i \cos[\Omega(t_n - \tau_{90})] - \frac{e}{2c}a_x \sin i \sin[2\Omega(t_n - \tau_{90}) - \omega_p] \quad (1)$$

where P is the pulse period at time t_0 , \dot{P} is the pulse period derivative, $a_x \sin i$ is the projected semimajor axis of the orbit of the neutron star, τ_{90} is a reference time, which for a circular orbit corresponds to superior conjunction, Ω is the orbital frequency which we fix at a value of $2\pi/4.400 \text{ radians day}^{-1}$, and ω_p is the longitude

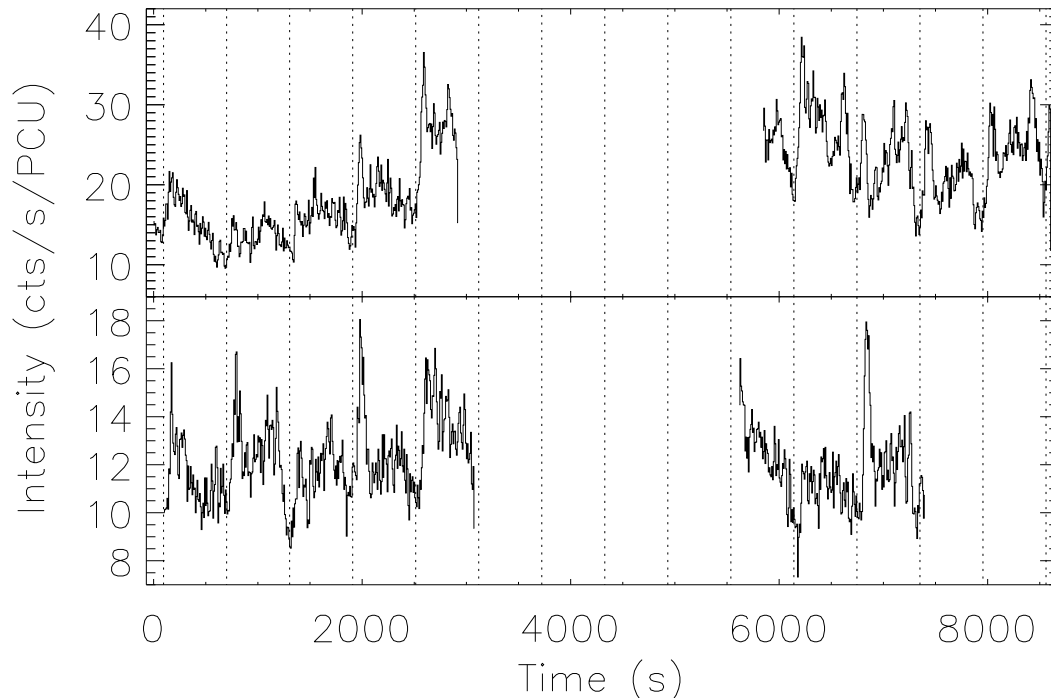


FIG. 1.— PCA counting rate data for the 3.7–17 keV energy band in 8-s time bins for two representative observations of X1908+075, i.e., the observations of 2002 December 23 (bottom; Obs. ID 70083-01-01-00) and of 2003 February 8 (top; Obs. ID 70083-02-19-00). The vertical lines are drawn every 605 seconds and are roughly aligned with the principal minimum in the pulse profile. The gap in the middle of each observation is due to Earth occultation of the source. The non-source background rate is $\sim 7.5 \text{ cts s}^{-1} \text{ PCU}^{-1}$.

of periastron. The last term represents the first order term in a Taylor series expansion in the eccentricity e and is a reasonable approximation for a mildly eccentric orbit. The curve representing the best-fit orbit and pulse period behavior is shown superposed on the arrival time delays in Fig. 3. The rms scatter of the arrival time delays about this best fit curve was found to be $\sim 6 \text{ s}$ and was used as an empirical estimate of the uncertainty in the individual arrival times. This was the basis on which we derived formal confidence limits on the individual fitted parameters.

The results of this fit are given in Table 2. The value of $a_x \sin i$ of 47.8 lt-s , combined with an orbital period of 4.4 days, yields a mass function of $6.07 \pm 0.35 M_\odot$. This points to a fairly massive companion star. The best-fit orbital eccentricity is $e = 0.021 \pm 0.039$, and, therefore, the orbit is consistent with being circular. We set a 2σ upper limit $e < 0.1$. The pulse period, after corrections for orbital motion of the Earth and of the pulsar, is determined to be $P = 604.684 \pm 0.001 \text{ s}$ at $t = \text{MJD } 52643.3$. The pulse period derivative is found to be positive, $\dot{P} = (1.22 \pm 0.09) \times 10^{-8}$, and thus the neutron star rotation is slowing down. Expressed as a fractional rate,

we obtain $\dot{P}/P \simeq 6.4 \times 10^{-4} \text{ yr}^{-1}$.

In Fig. 4 we show the measured pulse arrival time delays for the extensive 2002–2003 epoch 2 data set relative to our best-fit model excluding the orbital Doppler shift terms. The results are plotted modulo the 4.4-day orbital period. The solid curve is the best fit circular orbit with $a_x \sin i = 47.8 \text{ lt-s}$.

A similar pulse phase analysis was then carried out on the smaller epoch 1 data set taken approximately two years earlier. Only 7 of the pulse arrival time delays from this earlier set proved to be useful in the model fitting, in part because it was difficult to unambiguously connect the pulse phase across the large gap between the two subsets of epoch 1 observations. The Doppler delays for these 7 arrival times, which span only one orbital cycle, are plotted in Fig. 5. When fitting these delays, we fixed the amplitude ($a_x \sin i$) at the value determined from the later, more extensive observations, which yield much more accurate orbital parameters. The orbital period (P_{orb}) was fixed at the value determined previously from 3 years of ASM observations (WRB). The main objective in using these observations was to determine a relatively accurate orbital phase some two years before

TABLE 1
X1908+075 PULSE ARRIVAL TIME DELAYS

Observation ID	Time of Obs. ^a (MJD)	Exposure (s)	Count Rate ^b (cts s ⁻¹)	Orb. Phase ^c (cycles)	Pulse Time ^d Delay (s)
70083-01-01-00	52631.1289	3344	7.79	0.942	-0.2
70083-01-02-00	52631.6400	1488	12.30	0.058	1.4
70083-01-02-01	52631.7077	1440	21.77	0.074	-1.4
70083-01-03-00	52632.1150	3424	16.24	0.166	-25.2
70083-01-04-00	52632.7296	1200	8.38	0.306	-71.3
70083-01-05-00	52633.3469	2448	15.19	0.446	-80.6
70083-01-05-01	52633.4084	1312	22.48	0.460	-99.5
70083-01-06-01	52633.6143	1856	12.29	0.507	-98.4
70083-01-06-00	52633.7382	3216	14.14	0.535	-94.4
70083-01-07-00	52634.2994	2816	10.10	0.663	-74.0
70083-01-08-00	52634.8365	1200	9.68	0.785	-40.9
70083-01-09-01	52635.5223	2016	5.12	0.941	2.1
70083-01-10-00	52635.8639	3312	8.31	0.018	-15.7
70083-01-11-01	52636.3726	2080	7.18	0.134	-20.9
70083-01-11-00	52636.5098	2032	4.96	0.165	-28.4
70083-01-12-01	52636.9702	1888	7.55	0.270	-50.7
70083-01-12-00	52637.0396	1520	10.89	0.285	-64.2
70083-01-13-00	52637.3282	2784	12.79	0.351	-93.1
70083-01-14-00	52637.9570	1776	13.97	0.494	-110.9
70083-01-14-01	52638.0480	1408	29.83	0.515	-105.1
70083-01-15-00	52638.4150	2240	14.51	0.598	-98.5
70083-01-15-01	52638.4827	2384	17.15	0.613	-84.8
70083-01-16-01	52638.8809	1008	16.73	0.704	-81.6
70083-01-16-00	52638.9476	1008	23.72	0.719	-61.5
70083-01-16-02	52639.0372	1168	19.72	0.739	-63.2
70083-01-17-00	52639.5570	2864	12.72	0.857	-32.3
70083-01-18-00	52640.0893	3232	11.46	0.978	-11.0
70083-01-19-00	52640.3903	2672	11.24	0.047	-13.6
70083-01-19-01	52640.5146	1904	17.32	0.075	-25.8
70083-01-20-00	52641.0247	2960	14.42	0.191	-41.4
70083-01-21-00	52641.4070	2720	21.03	0.278	-72.3
70083-01-22-00	52641.8042	2192	12.16	0.368	-90.0
70083-01-23-00	52642.4619	2816	16.83	0.518	-114.8
70083-01-24-00	52642.9233	1632	12.85	0.622	-88.2
70083-01-25-00	52643.2959	1088	15.11	0.707	-68.2
70083-01-26-00	52643.7705	2608	12.80	0.815	-41.1
70083-01-27-00	52644.1608	3408	8.86	0.904	-19.4
70083-01-28-00	52644.8823	2624	9.46	0.068	-16.1
70083-02-01-00	52669.1497	3536	13.09	0.582	-67.8
70083-02-01-01	52669.2184	1808	17.62	0.598	-73.9
70083-02-02-00	52669.7313	1648	17.05	0.714	-43.0
70083-02-02-01	52669.7997	2080	10.21	0.730	-36.8
70083-02-03-00	52670.1434	2112	19.80	0.808	-15.5
70083-02-03-01	52670.2066	1904	13.94	0.822	-7.3
70083-02-04-00	52670.7184	1600	11.88	0.938	22.0
70083-02-04-01	52670.7955	1952	13.91	0.956	16.8
70083-02-05-00	52671.1230	2640	8.26	0.030	16.8
70083-02-05-01	52671.1966	2432	19.39	0.047	17.1
70083-02-06-01	52671.7737	1824	8.30	0.178	1.8
70083-02-06-00	52671.8487	3408	9.06	0.195	-2.3
70083-02-07-00	52672.1834	2480	16.99	0.271	-36.6
70083-02-07-01	52672.2507	1856	14.01	0.287	-18.4
70083-02-08-01	52672.6924	1344	12.90	0.387	-61.1
70083-02-08-00	52672.7608	1728	11.97	0.403	-54.3
70083-02-09-00	52673.1705	2560	27.88	0.496	-60.3
70083-02-10-02	52673.5744	944	9.03	0.587	-59.2
70083-02-10-01	52673.6796	1312	14.04	0.611	-57.3
70083-02-10-00	52673.7573	1792	18.22	0.629	-44.0
70083-02-11-00	52674.1903	2560	9.01	0.727	-13.5
70083-02-12-00	52674.7445	1680	6.08	0.853	25.7
70083-02-12-01	52674.8198	1872	9.37	0.870	18.5
70083-02-13-00	52675.1768	2688	5.23	0.952	41.5
70083-02-14-00	52675.7355	2112	17.71	0.079	38.7
70083-02-14-01	52675.8025	2528	11.68	0.094	37.2
70083-02-15-00	52676.1636	2688	10.81	0.176	19.9
70083-02-16-00	52676.6994	1120	11.96	0.298	-18.3
70083-02-17-00	52677.0792	3456	10.55	0.384	-35.3
70083-02-18-00	52677.6855	1232	10.86	0.522	-43.8
70083-02-19-00	52678.0684	3296	9.68	0.609	-33.1

^aMidpoint of observation, MJD = JD - 2,400,000.5.

^bSource count rate (2-30 keV) using PCU No. 2. For reference, 1 Crab = 2500 cts s⁻¹.

^cOrbital phase corresponding to the observation midpoint calculated assuming $P_{\text{orb}} = 4.4007$ d and the time of phase zero $\tau_{90} = \text{MJD } 52631.383$.

^dPulse arrival time delay at the Solar System barycenter with respect to a clock with constant period $P = 604.689$ s.

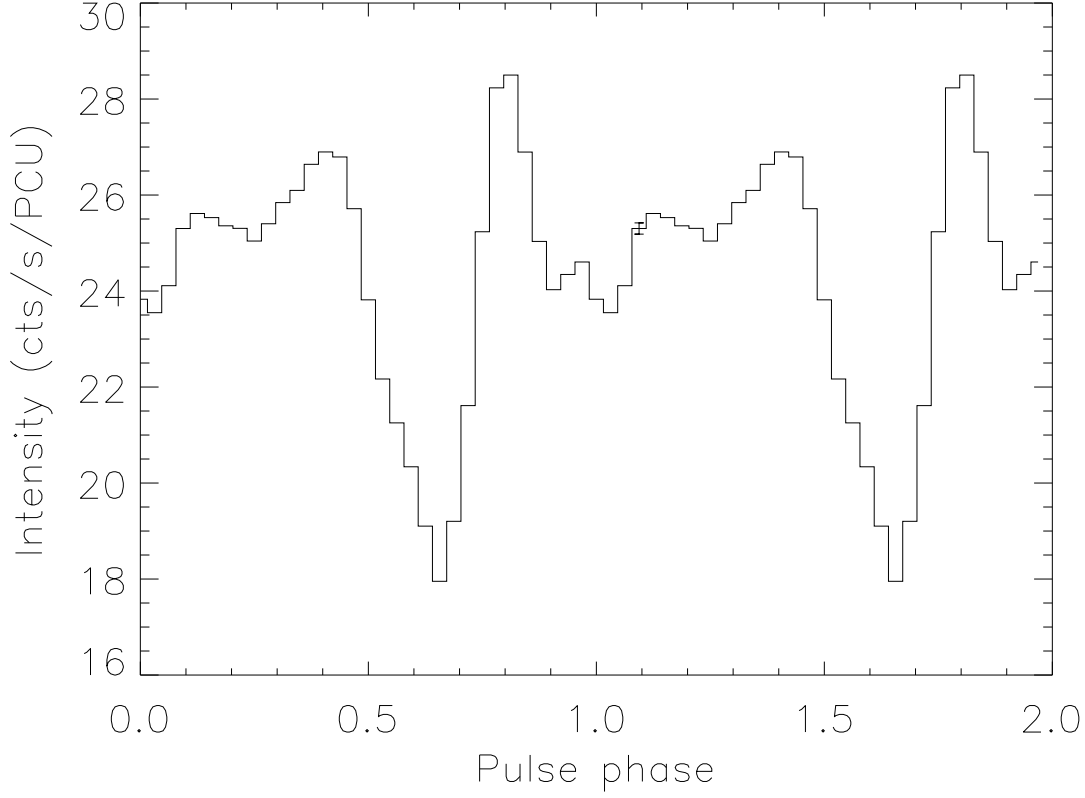


FIG. 2.— Pulse profile template used for computing the cross correlation function. The profile is shown for two cycles. The error bar shows the approximate uncertainty ($\pm 1 \sigma$) from variations of the source intensity at a given pulse phase within a typical observation. Fluctuations due to counting statistics are negligible. The non-source background rate is $\sim 7.5 \text{ cts s}^{-1} \text{ PCU}^{-1}$.

TABLE 2
RESULTS OF THE TIMING ANALYSIS

Parameter	2nd-Epoch Parameter ^a	1st-Epoch Parameter ^b	Comments
$a_x \sin i$ (lt-s)	47.83 ± 0.94	47.83 (fixed)	
τ_{90} (MJD)	52631.383 ± 0.013	51870.06 ± 0.15	superior conjunction for circular orbit at MJD 52643.3, 51870, respectively
P (s)	604.684 ± 0.001	604.660 ± 0.040	
\dot{P} (s s^{-1})	$(1.22 \pm 0.09) \times 10^{-8}$	0 (fixed)	
e	0.021 ± 0.039	0 (fixed)	< 0.1 (2σ)
P_{orb} (days)	4.4007 ± 0.0009	4.4007 ± 0.0009	determined from both epochs jointly
$f(M)(M_{\odot})$	6.07 ± 0.35	NA	

^aBased on 69 pulse arrival times obtained from 2002 December 23 through 2003 February 8. Errors cited are single-parameter 1σ confidence limits.

^bBased on 7 pulse arrival times obtained from 2000 November 19 through 2000 November 23. Errors cited are single-parameter 1σ confidence limits.

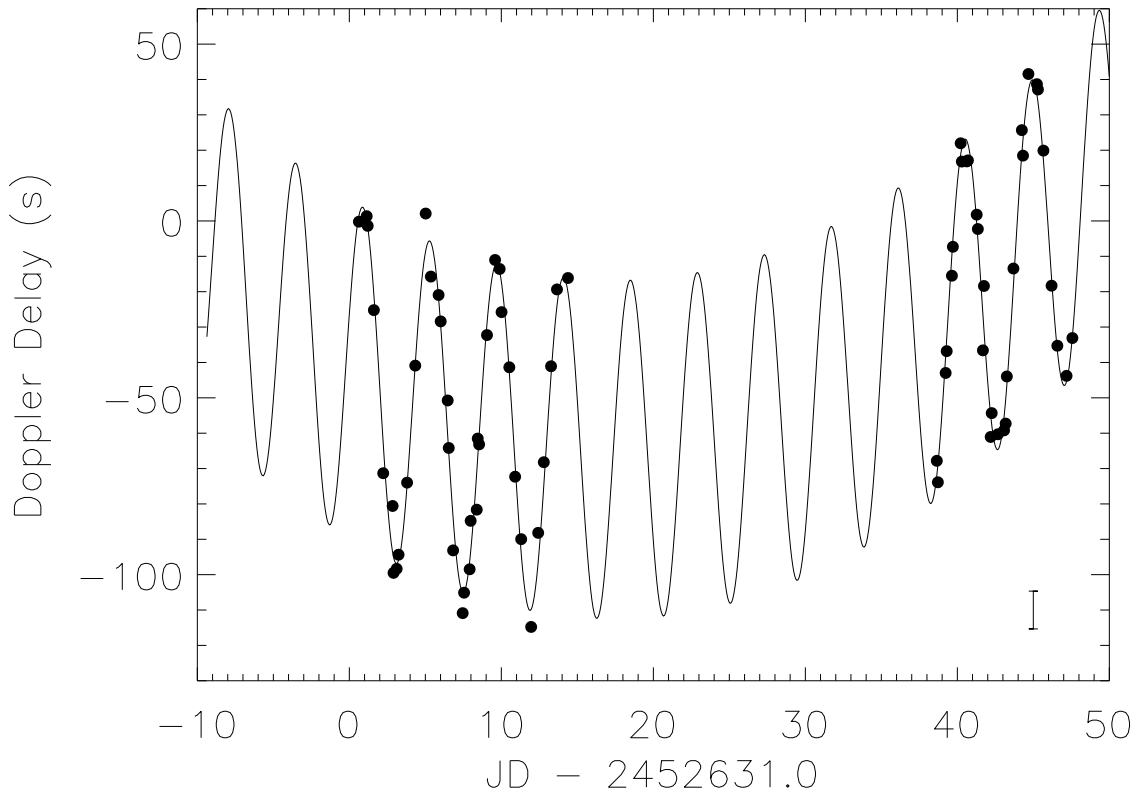


FIG. 3.— Pulse arrival time delays for 69 pointed observations made during the interval 2002 December 23 through 2003 February 8. The delays are computed relative to a reference pulse ephemeris that has a constant 604.689 s period at the Solar System barycenter. The curve shows the arrival time delays predicted by the best-fit model pulsar with a constant pulse period derivative moving in a circular orbit (see Table 2). A $\pm 1 \sigma$ error bar, estimated from the rms deviation of the measurements relative to the curve, is plotted in the lower right corner.

the later, more extensive observations. The two orbital phase determinations, separated by ~ 2 years, are then combined to compute a more accurate determination of the orbital period, $P_{\text{orb}} = 4.4007 \pm 0.0009$ days. This is consistent with, and of comparable precision to, the orbital period of 4.400 ± 0.001 days determined from the ASM X-ray light curve by WRB.

By now (2004 April), the ASM has accumulated $\sim 40,000$ individual intensity measurements of X1908+075 over ~ 8 years. This is more than twice the amount of data contained in the original light curve of WRB. We have therefore redone the light curve analysis using all the presently available ASM data to derive a new X-ray intensity-based value for the orbital period. Our result is $P_{\text{orb}} = 4.4006 \pm 0.0006$ days. This is consistent with the earlier result of WRB and with our pulse-timing-based result as well. The folded ASM light curves are shown in Fig. 6.

4. ORBITAL PHASE-DEPENDENT SPECTRAL ANALYSIS

The X-ray intensity of X1908+075 is strongly modulated with orbital phase. A qualitative feeling for the energy-dependence of the modulation can be obtained

from the folded ASM data (Fig. 6). The ASM light curves are extremely well sampled both as a function of orbital phase and over many orbital cycles. We define the degree of modulation as $(I_{\text{max}} - I_{\text{min}})/(I_{\text{max}} + I_{\text{min}})$, where I_{max} and I_{min} are the maximum and minimum intensities observed in the light curves. The degrees of modulation are found to be 0.41 ± 0.18 , 0.70 ± 0.15 , and 0.38 ± 0.04 for the 1.5 – 3, 3 – 5, and 5 – 12 keV energy bands, respectively. The uncertainties have been estimated primarily on the basis of statistical fluctuations in I_{min} , and do not include any contributions due to possible systematic baseline offsets. Nonetheless, we take these numbers, as well as the different shapes of the folded light curves, to be evidence of energy dependence of the orbital modulation.

In spite of the fact that the orbital light curves produced with the ASM are very well sampled, the energy resolution (limited to 3 channels) and calibration are not good for determining detailed spectral parameters. The PCA data are better suited to this purpose.

To help guide the spectral analysis, we consider the overall average spectrum of X1908+075 during the epoch 1 and epoch 2 *RXTE* pointed observations. In each case,

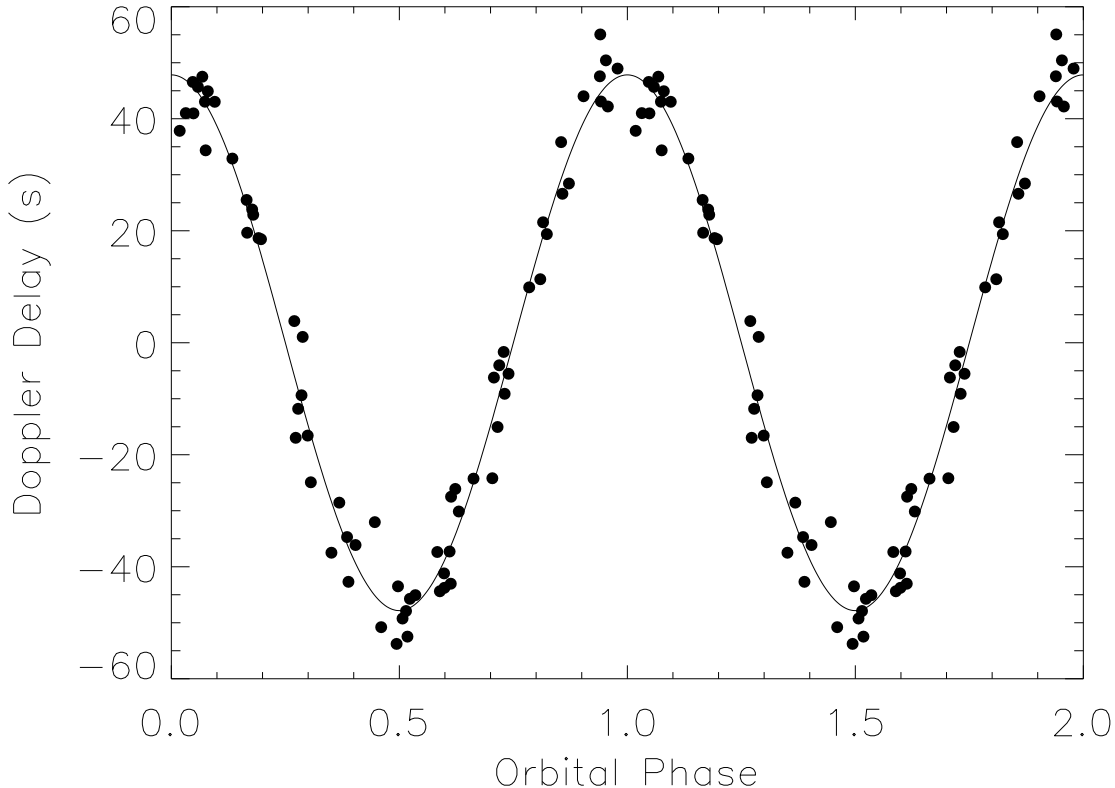


FIG. 4.— Doppler delay curve for the same set of observations as shown in Fig. 3 but plotted as a function of orbital phase. Each measurement is plotted twice in order to show two complete orbital cycles. The quadratic term representing the change in intrinsic pulse period, evident in Fig. 3, has been removed. The curve represents the best-fit circular orbit.

the PCA spectrum (2-25 keV; PCU 2) shows evidence of low-energy attenuation by a substantial column density and the presence of line emission due to neutral or ionized Fe at energies of approximately 6.4-6.7 keV. The HEXTE spectrum (both clusters) in the range 15-70 keV shows a high-energy cutoff that rules out a simple power-law model. For both epochs, thermal bremsstrahlung and cutoff power-law models yield reasonable fits of the continuum spectrum. We proceed with the bremsstrahlung model since it has fewer free parameters, gives results for each epoch that are remarkably consistent, and (in hindsight) gives best-fit temperatures from the individual observations that agree well with each other. Since the spectral resolution of the PCA is at best marginal for determination of the Fe line energy, we assume that any line emission near these energies is at 6.7 keV; this should be an adequate model of the Fe line region for the present purposes. The fit of the average spectrum from epoch 1 (35 ks of exposure) yields a column density $N_H = (1.12 \pm 0.02) \times 10^{23} \text{ cm}^{-2}$, a temperature $kT = 23.3 \pm 0.5 \text{ keV}$, and a value of chi-square per degree of freedom $\chi^2_\nu = 2.42$. The fit of the spectrum from 153 ks of exposure in epoch 2 yields $N_H = (1.22 \pm 0.02) \times 10^{23} \text{ cm}^{-2}$, $kT = 22.6 \pm 0.3 \text{ keV}$, and $\chi^2_\nu = 4.84$. These values

for χ^2_ν are formally unacceptable. However, the average spectra comprised data obtained from large accumulated exposure times so that the uncertainties from counting statistics are very small. In fact, in our analysis of the PCA spectral data we estimated the error for each energy bin by adding the statistical error in quadrature with a presumed 1% systematic error which represents the uncertainty in the instrument response function (e.g., Sobczak et al. 2000). For much of the energy range these presumed systematic errors dominate the statistical errors. Perhaps most importantly with regard to the χ^2 values of the fits of the average spectra, the N_H values vary significantly from observation to observation. In such a case, a model based on a single value for N_H cannot be expected to precisely fit the average spectrum.

Next, we analyzed the net spectrum for each of the 69 epoch 2 pointed observations for which we have determined a pulse arrival time. The analysis was repeated for each of three spectral models in order to estimate how the formal statistical uncertainties compare with those due to the particular choice of model. Each model is intended to provide a simple spectral shape that is likely to fit the data well and to yield a good estimate of the low-energy absorption. All the models involved a thermal

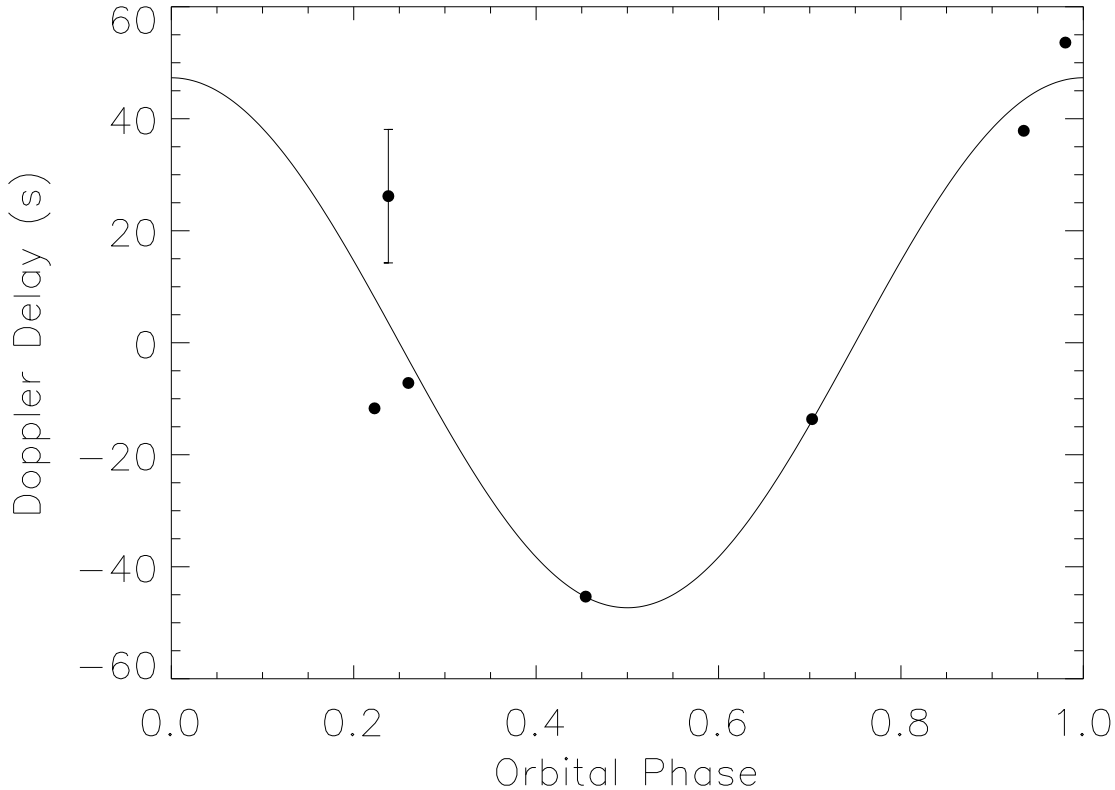


FIG. 5.— Seven pulse arrival time delays for observations during 2000 November (approximately two years prior to the more extensive observations shown in Fig. 3). These data spanned only one orbital cycle of X1908+075. The curve represents the best-fit circular orbit (see text). The uncertainty in the arrival time delay ($\pm 1\sigma$), estimated from the rms deviation of the measurements relative to the curve, is shown as an error bar on one of the measurements.

bremsstrahlung spectrum, a 6.7 keV iron line (which, as noted above, also represents line emission near 6.4 keV), and absorption by the interstellar medium (ISM) and a stellar wind.

Inspection of the raw pulse height spectra reveals that there are ‘excess’ counts at low energy (i.e., $\lesssim 6$ keV) with respect to the energy dependence expected from photoelectric absorption in a neutral gas. Two possible explanations of this form of the low-energy portion of the spectra immediately arise. First, the observed spectrum could be formed by both X-rays that propagate directly to the detectors along paths that pass close to the companion star and therefore are heavily attenuated, as well as X-rays that are scattered farther out in the stellar wind and are not attenuated so heavily by photoelectric absorption. Second, if the stellar wind is partially ionized, then the energy dependence of any absorption will not be as strong as that for strictly neutral gas. The combination of these effects can be approximately taken into account by allowing the presence of two spectral components that are attenuated by different amounts.

We take the intrinsic emission spectrum of the source

to be

$$S(E) = C_1 Br(E, kT) + C_2 G(E) \quad (2)$$

where $Br(E, kT)$ represents an optically thin thermal bremsstrahlung spectrum characterized by temperature T and $G(E)$ represents a Gaussian profile line centered at 6.7 keV with width $\Delta E(1\sigma) = 0.3$ keV. This is used, in turn, in a generic spectral model:

$$F_x = \exp[-N_{H_{\text{ISM}}}\sigma(E)] \times \{C_3 \exp[-N_{H_{\text{wind}}}\sigma(E)] + (1 - C_3)\} S(E) \quad (3)$$

C_1 , C_2 , and C_3 are parameters of the model. Each of the three spectral models that we apply to the observations uses a particular form of this generic model. In Model 1, the thermal bremsstrahlung spectrum is attenuated by the ISM and a stellar wind, kT is free to vary from one observation to another, and C_3 is assigned a value of one. The ISM and wind column densities are not determined separately; only their sum is determined. Model 2 is the same as Model 1, except that kT is fixed at the value of 22.6 keV that was determined by the fit of the average spectrum of the epoch 2 observations. Model 3 is similar to Model 2, except that the absorption is characterized

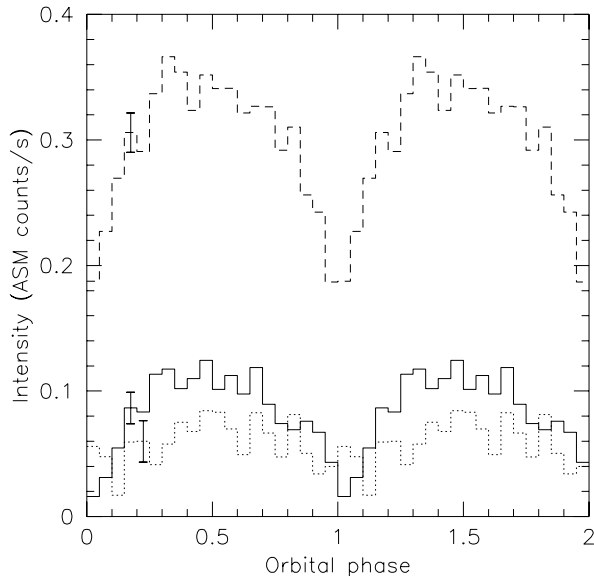


FIG. 6.— Average intensity as a function of orbital phase produced by folding ~ 8 years of ASM results at the period $P = 4.4006$ days. The dotted, solid, and dashed histograms correspond to the (nominal) 1–3.5, 3.5–5, and 5–12 keV energy bands. Each curve is shown for two cycles. For each of these energy bands, an intensity of 1 ASM count s^{-1} corresponds to ~ 40 mCrab.

by ‘partial covering’ and so the parameter C_3 is determined for each observation. For Models 1 and 2, the free parameters were simply determined by varying the free parameters so as to minimize the χ^2 statistic. For Model 3 such a procedure did not yield acceptable results, so an iterative procedure was used. In this procedure, the value of $N_{H\text{ISM}}$ was fixed and the remaining free parameters including $N_{H\text{wind}}$ were determined for each observation by a minimum χ^2 fit with XSPEC. A fit of a model of the orbital phase dependence of $N_{H\text{wind}}$ was then made to the resulting $N_{H\text{wind}}$ values to determine wind parameters (with $\beta = 0$, see §5 below). Then the spectral fit of each observation was redone using XSPEC with $N_{H\text{ISM}}$ as a free parameter and with the value of $N_{H\text{wind}}$ fixed to the value predicted from the fit of the wind parameters. The weighted mean of the $N_{H\text{ISM}}$ values then was used as a revised estimate of this quantity. This entire procedure was iterated 4 times to obtain convergence. In the final iteration, $N_{H\text{ISM}}$ was set to 4.6×10^{22} atoms cm^{-2} , which indicates that substantial absorption occurs in the ISM (although it should be noted that this column density is, at all orbital phases, comparable or smaller than that in the stellar wind).

The statistics of the individual observations were not sufficient to conclude that one of the spectral models fit the data significantly better than the other models. Rather, all three models yield comparable quality fits with reduced χ^2 values in the range 0.5–2.0 for all but a few observations. As might be expected, the value of the normalization constant C_1 does not appear to be dependent on orbital phase, but the iron line intensity does appear to depend on orbital phase by as much as 30% in the Model 2 results and less in the Model 1 and Model 3 results. In the Model 3 fit results, the value of C_3 , the

covering fraction, is always in the range 0.4–1.0 and, for $\sim 85\%$ of the observations, is in the range 0.85–1.0.

The total neutral hydrogen column densities ($N_H = N_{H\text{ISM}} + N_{H\text{wind}}$) for the 69 observations are shown as a function of time in Fig. 7; the top panel shows results from spectral Model 1, while the bottom panel shows those for the partial covering model (Model 3). Note the pronounced variation of N_H with maxima at the expected orbital phases. A comparison of the two panels provides an idea of the sensitivity of N_H to the choice of spectral model; spectral Model 2 yields qualitatively similar results. The fitted values of N_H based on Models 1 and 3 are also plotted modulo the orbital phase in Figure 8.

The average spectrum from seven observations performed at orbital phases when the column density is expected to be high, i.e., $|\phi_{\text{orb}}| < 0.12$, is shown in the top and middle panels of Figure 9. The degree of low energy attenuation contrasts with that of the spectrum from eight observations performed at orbital phases when the column density is expected to be low (Fig. 9, lower panel). We have fit each average spectrum with both Models 2 and 3, but we fixed the value of the bremsstrahlung temperature in each case to that determined from the average spectrum of all the epoch 2 observations. We also fixed the energy of the Gaussian line center at 6.7 keV and the line width at $\sigma_{\text{line}} = 0.3$ keV. The results are given in Table 3. The Model 2 best-fit high N_H spectrum and the Model 3 best-fit low and high N_H spectra are also shown in Fig. 9. The plots illustrate the low energy attenuation and its variation. Spectral features are quite apparent at ~ 7 keV; these comprise Fe K line emission and absorption edges. The iron absorption is particularly prominent in the high N_H spectrum. Both the low and high N_H spectra are fit somewhat better by Model 3, although neither model fits the data well; the values of reduced χ^2 are significantly above 1.

From the spectral fits, we find that the X-ray flux, averaged over an observation and adjusted for low-energy absorption, is most often in the range $F_X(2\text{--}30 \text{ keV}) \sim 3\text{--}8 \times 10^{-10}$ ergs $\text{cm}^{-2} \text{ s}^{-1}$. Thus the X-ray luminosity of X1908+075 is typically $L_X(2\text{--}30 \text{ keV}) \sim 2\text{--}6 \times 10^{36} (D/8 \text{ kpc})^2$ ergs s^{-1} where D is the distance to the source, and, even at the high end of this range, is far below the Eddington limit for a $1.4 M_\odot$ neutron star, i.e., $L_{\text{Edd}} = 2.0 \times 10^{38}$ ergs s^{-1} . This is consistent with the picture that the neutron star is accreting from a wind from the companion star rather than being fed via Roche lobe overflow.

5. ABSORPTION IN A STELLAR WIND AND THE BINARY SYSTEM

The variation of the column density with orbital phase is caused by the movement of the X-ray source through the stellar wind of the companion star which is likely a spatially and temporally complex medium. In order to estimate the orbital inclination as well as other orbital parameters and properties of the companion star, we proceed by modelling the column density variation as orbital-phase dependent absorption in a spherically symmetric and temporally constant wind from the companion star.

The wind from an early-type star is often mod-

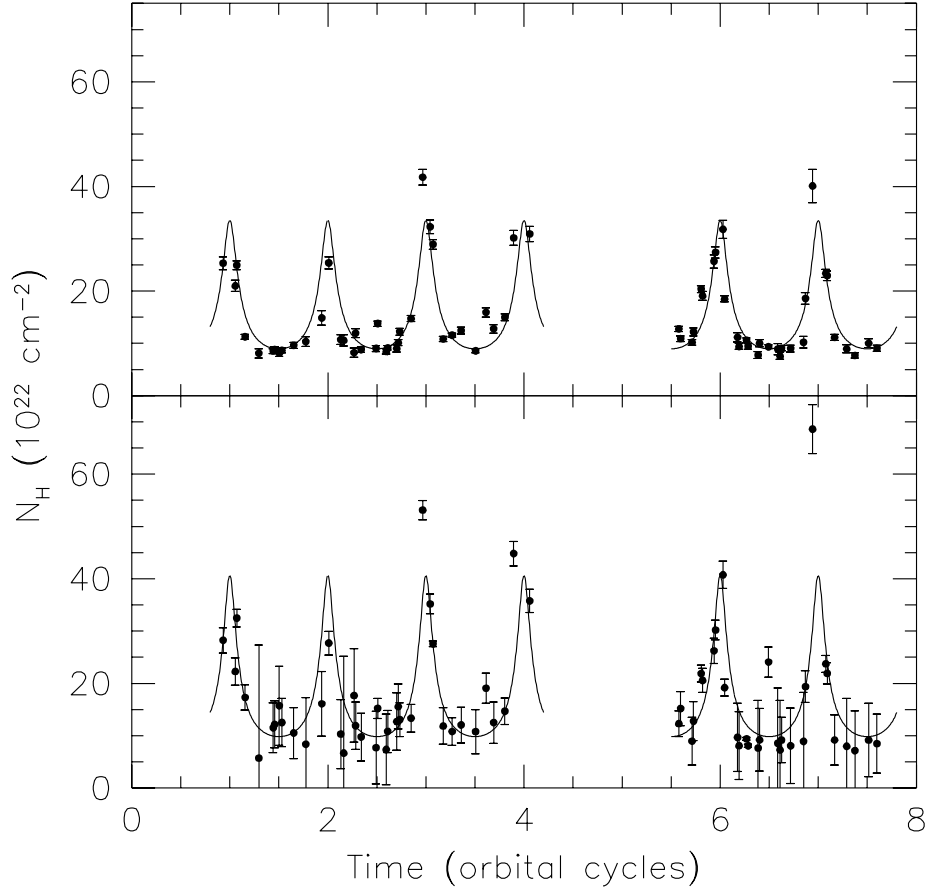


FIG. 7.— Estimates of $N_H = N_{H_{\text{wind}}} + N_{H_{\text{ISM}}}$ derived from spectral fits plotted as a function of time expressed in units of orbital cycles. Integral values of time, i.e., the times of orbital phase zero, correspond to superior conjunction of the neutron star. The upper plot shows estimates derived from fits of spectral Model 1 with uncertainties ($\pm 1 \sigma$) taken from the XSPEC fits. The lower plot shows estimates from spectral Model 3 with uncertainties ($\pm 1 \sigma$) taken from those for $N_{H_{\text{wind}}}$ from the final set of XSPEC runs since we assume the uncertainty in $N_{H_{\text{ISM}}}$ may be neglected in this case. The curves show the best fits of the orbital-phase dependent column density with $\beta = 0$; the best-fit curve for $\beta = 1$ (see text) is nearly indistinguishable from the curve shown here. For this plot, the long gap between sets of observations was artificially shortened by 4.0 orbital cycles.

elled as a steady-state, spherically symmetric flow at a velocity that gradually increases from zero to a terminal velocity of order of magnitude $\sim 1000 \text{ km s}^{-1}$. The wind density profile then follows from the assumption of a radius-independent mass flux (Lucy & Solomon 1970; Castor, Abbott, & Klein 1975; Lamers & Cassinelli 1999, and references therein). For our purposes the radial flow velocity may be taken to be

$$v(r) = v_\infty (1 - R_c/r)^\beta \quad (4)$$

where r is the distance from the center of the companion star, v_∞ is the wind terminal velocity, R_c is the radius of the companion star, and β is often in the range 0.7–1.2 for early-type stars (e.g., Groenewegen & Lamers 1989; Puls et al. 1996). The wind density profile then follows from the conservation of mass:

$$n(r) = \frac{n_0 (1 - R_c/a)^\beta}{(r/a)^2 (1 - R_c/r)^\beta} \quad (5)$$

where $n(r)$ is the number density of hydrogen atoms in the stellar wind at the distance r from the companion

star and n_0 is the number density at the distance a . For a circular orbit with orbital inclination angle i , the instantaneous column density of material between the neutron star and the observer, N_H , is given by:

$$N_H = N_{H_{\text{ISM}}} + N_{H_{\text{wind}}} = N_{H_{\text{ISM}}} + \int_0^\infty n[r(s)] ds \quad (6)$$

$$= N_{H_{\text{ISM}}} + a n_0 (1 - R_c/a)^\beta \int_0^\infty \frac{ds'}{r'^2 (1 - R'_c/r')^\beta} \quad (7)$$

where $N_{H_{\text{ISM}}}$ and $N_{H_{\text{wind}}}$ are the separate contributions from the interstellar medium and the stellar wind, respectively, s is the distance along the line from the neutron star toward the observer, and primed quantities are normalized relative to a .

The radial distance r is a function of the distance s and the angle ϕ subtended at the neutron star between the direction to the observer and the radial direction. In terms of normalized quantities, we have

$$r'^2 = 1 + s'^2 - 2s' \cos \phi. \quad (8)$$

The angle ϕ , in turn, is related to the inclination angle

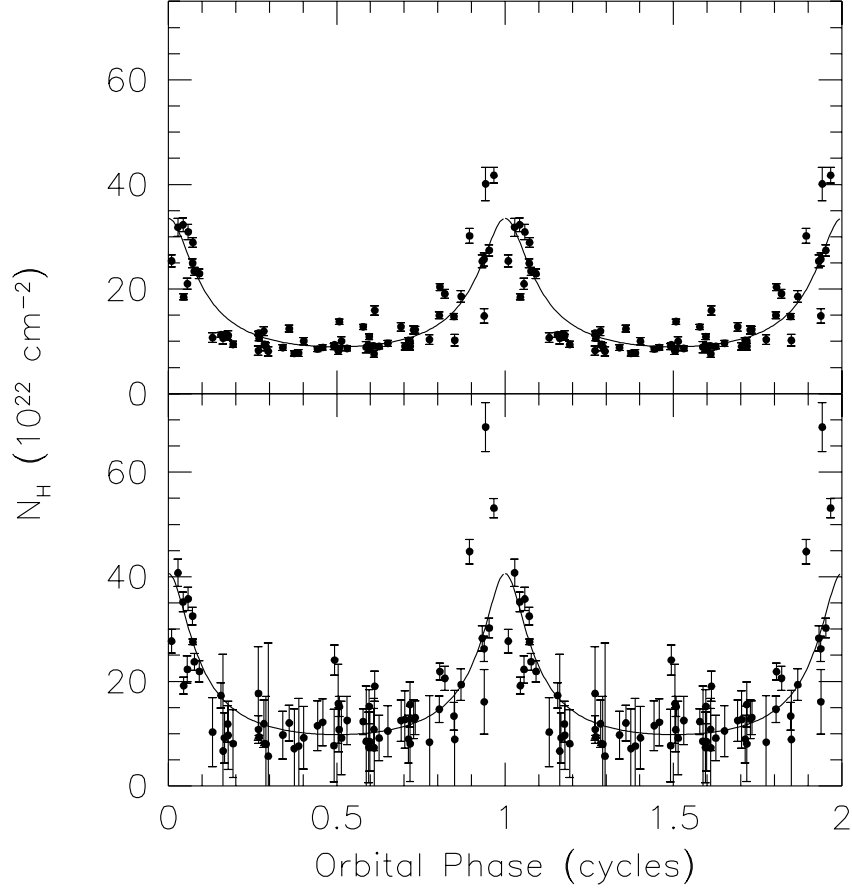


FIG. 8.— (top) N_H estimates for spectral Model 1 as a function of orbital phase. The points shown are those shown in the top panel of Fig. 7. (bottom) N_H estimates for spectral Model 3. In both panels, the solid curve shows the best-fit $\beta = 0$ stellar wind model. As noted in Fig. 7, the best-fit curve for the $\beta = 1$ model is nearly indistinguishable. The points and curves are shown in each of two cycles.

TABLE 3
SPECTRAL FIT RESULTS

Parameter	Low N_H Model 2	Low N_H Model 3	High N_H Model 2	High N_H Model 3
C_1^a	0.1012 ± 0.0004	0.1023 ± 0.0005	0.0880 ± 0.0004	0.0905 ± 0.0005
C_2^b	5.7 ± 1.1	6.1 ± 1.1	3.3 ± 1.0	4.8 ± 1.1
$N_{H\text{ISM}}^c$		4.7 (fixed)		4.7 (fixed)
$N_{H\text{wind}}^c$		8.5 ± 1.3		24.7 ± 0.7
$N_{H(\text{total})}^c$	9.3 ± 0.1		24.3 ± 0.2	
C_3 (covering fraction)		0.66 ± 0.06		0.916 ± 0.008
χ^2	126.2	115.0	222.3	142.5
Degrees of freedom	46	45	46	45
χ^2_ν	2.74	2.56	4.83	3.17

NOTE. — All quantities are defined in eqs. 2 and 3. For all 4 fits, the bremsstrahlung temperature was fixed at $kT = 22.6$ keV, the spectral line center energy was fixed at 6.7 keV and the line width fixed at $\sigma = 0.3$ keV. The low N_H spectrum is the average from 8 observations. The high N_H spectrum is the average from 7 observations (see text).

^aNormalization factor for XSPEC component “bremss” to give flux in units of photons $\text{cm}^{-2} \text{s}^{-1} \text{keV}^{-1}$

^bIron line flux in units of 10^{-4} photons $\text{cm}^{-2} \text{s}^{-1}$

^cIn units of 10^{22} H-atoms cm^{-2}

and the orbital phase by:

$$\cos \phi = -\sin i \cos[\Omega(t - \tau_{90})] . \quad (9)$$

For the simple case of an inverse square law density profile, i.e., $\beta = 0$, the wind column density integral equals

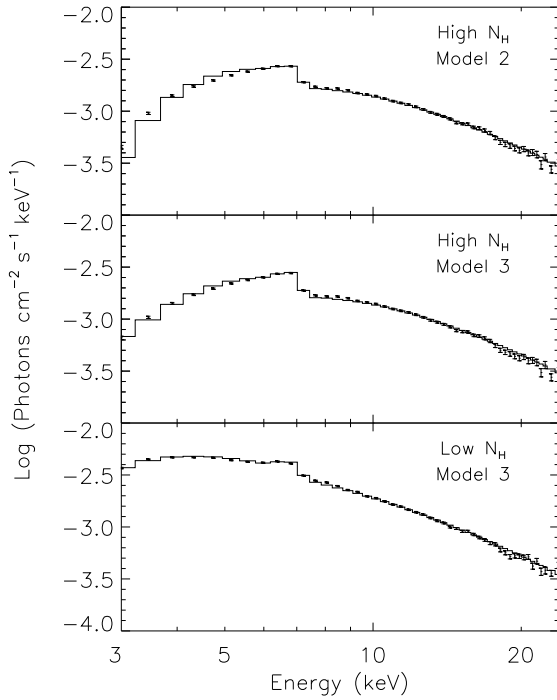


FIG. 9.— Inferred photon number spectra (points with error bars) of the accumulated data from 7 observations when the absorbing column density was inferred to be relatively high (top and middle panels), and of the data from 8 observations when the column density was relatively low (bottom panel). The histogram in the top panel shows the best-fit of the Model 2 spectrum while the histograms in the middle and lower panels show the best fit of the Model 3 spectrum.

$an_0\phi/\sin\phi$ if ϕ is given in radians. In this case, the wind column densities, in units of n_0a , are 1, $\pi/2$, $3\pi\sqrt{2}/4$, and ∞ for $\phi = 0, \pi/2, 3\pi/4$, and π radians respectively, and the ratio of maximum to minimum value is given simply by $N_{H_{\text{wind}}}(\text{max})/N_{H_{\text{wind}}}(\text{min}) = (\pi/2 + i)/(\pi/2 - i)$.

Since we know τ_{90} from our orbital analysis, there are 5 parameters that can potentially be determined from fits to the orbital modulation of N_H : i , β , R_c , $N_{H_{\text{ISM}}}$, and the product $an_0(1 - R_c/a)^\beta$. In the analysis procedure, for each of a set of assumed trial values for i , β , and R_c , we performed a linear least squares fit of the model defined by eq. (7) to the column densities determined from our Model 1 spectral fits, and thereby obtained values for $N_{H_{\text{ISM}}}$ and $an_0(1 - R_c/a)^\beta$ as well as an estimate of the root-mean-square deviation of the column densities from the fit. We have fit models for a wide range of orbital inclinations. For each trial value of i , we use our best-fit value for $f(M)$ (see Table 2) and assume that the mass of the neutron star is the canonical $1.4M_\odot$ to compute the mass of the companion M_c . Using the resulting mass ratio, i , and our best fit value for $a_x \sin i$, we then compute the orbital separation a . For the given inclination, the set of trial values of R_c covers a range up to a maximum value taken to be the smaller of the Roche lobe radius of

the companion star or the radius which would produce a grazing eclipse. Finally, for simplicity, we considered only three discrete values for the wind parameter β : 0, $1/2$, and 1.

Since we do not have any reliable way to estimate the uncertainties in the measured column densities due to systematic errors, we have taken the rms spread between the values found from the spectral analysis (for the 69 individual observations) and the best-fit model to be the 1σ error. When we do this, the minimum value of χ^2 should be 65, by definition, since there are 69 data points and 4 fitted parameters (not counting β). The contour at $\chi^2 \sim 65 + 4.6 = 69.6$ is then relevant for estimation of the 90% confidence region in the $i - R_c$ plane (with $N_{H_{\text{ISM}}}$ and $an_0(1 - R_c/a)^\beta$ treated as uninteresting parameters). In Fig. 10, we show contours of χ^2 in this plane from fits of the $\beta = 1$ model. We note that, in the limit of vanishing R_c , the value of β becomes irrelevant and the model is equivalent to the $\beta = 0$ model. Thus, the contours at small R_c in Fig. 10 indicate the acceptable range of inclinations in the $\beta = 0$ fits. We find that the best fits for each of the three values of β are very similar in quality, so we cannot discriminate among these values of β using this criterion alone.

The best fits of the $\beta = 1$ model to the values of N_H from spectral Models 1, 2, and 3 give rms observed-minus-calculated values of 4.1×10^{22} , 5.1×10^{22} , and 7.7×10^{22} H atoms cm^{-2} , respectively. The $\beta = 0$ and $1/2$ cases give slightly larger residuals. The best fit to the spectral Model 1 results of a $\beta = 0$ model is characterized by $i = 64.5^\circ$, $M_c = 11M_\odot$, $a = 60$ lt-s, $N_{H_{\text{ISM}}} = 4.1 \times 10^{22} \text{ cm}^{-2}$, and $N_{H_{\text{wind}}}(\phi = 0) = an_0 = 4.7 \times 10^{22} \text{ cm}^{-2}$. The best fit to the spectral Model 1 results of a $\beta = 1$ model has $i = 48.5^\circ$, $M_c = 17M_\odot$, $R_c = 16R_\odot$, $a = 69$ lt-s, $N_{H_{\text{ISM}}} = 5.0 \times 10^{22} \text{ cm}^{-2}$, and $N_{H_{\text{wind}}}(\phi = 0) = 3.6 \times 10^{22} \text{ cm}^{-2}$. The column densities predicted by these models are practically indistinguishable from each other; they are shown in Figs. 7 and 8. We emphasize that acceptable fits are obtained for a considerable range of parameters, and that the best-fit parameters given above are merely illustrative of the allowed values. Our estimates of the system parameters for X1908+075 are summarized in Table 4.

The results of the column density fits are shown as constraints on the companion star mass and radius in Fig. 11. and allow us to set, e.g., assuming $\beta = 1.0$, upper limits of $\sim 30M_\odot$ and $\sim 22R_\odot$ on the mass and radius, respectively, of the companion star. We note that for $M_c > 13.5M_\odot$, the upper limits on the companion radius correspond to the Roche lobe radius, while the lack of an apparent X-ray eclipse bounds the allowed radii for $M_c < 13.5M_\odot$. In Fig. 11 we also show the measured masses and radii of the companion stars in 6 well known high-mass X-ray binaries and mass-radius relations for zero-age main-sequence (ZAMS) stars, for stars that have exhausted half of the hydrogen at their centers, and for stars at the end of the main sequence phase of their evolution, i.e., the terminal-age main sequence (TAMS), where the mass is that indicated on the axis (Ph. Podsiadlowski 2004, private communication). These mass-radius relations were derived for single (isolated) stars neglecting the effects of any mass loss.

Each set of system parameters and wind density pro-

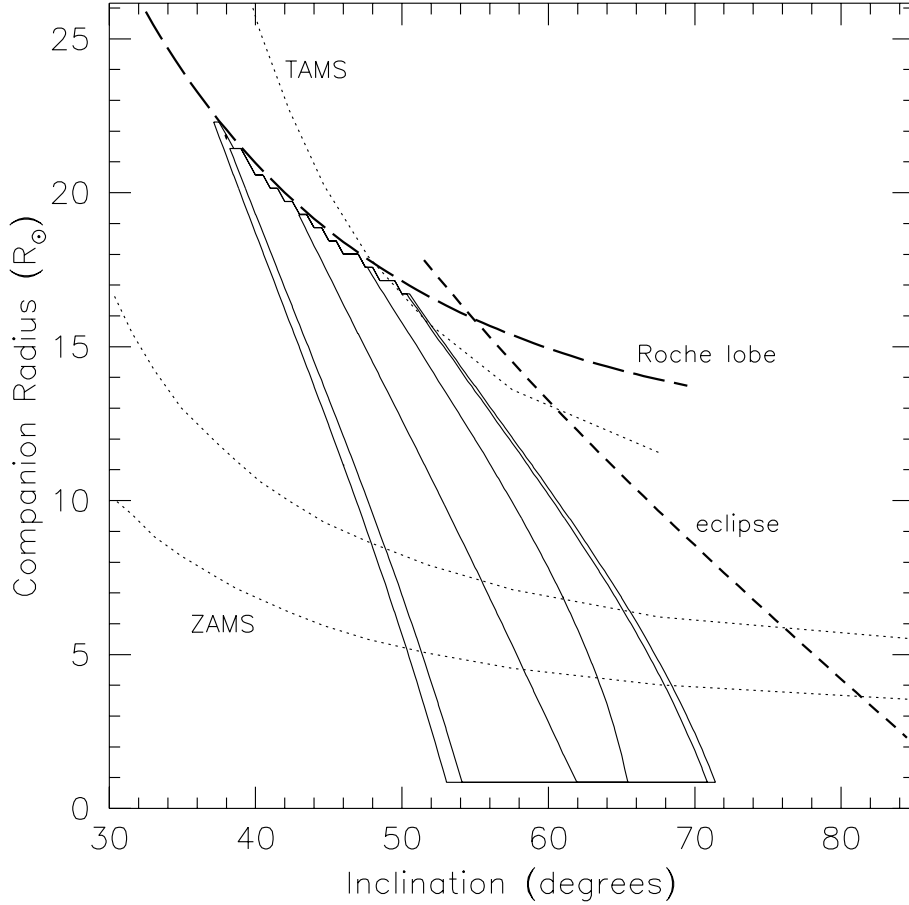


FIG. 10.— Contours (solid curves) of χ^2 in the $i - R_c$ plane from fits of the column densities for wind density profiles with $\beta = 1$ to the spectral Model 1 N_H measurements shown in the upper panel of Fig. 7. The three contours show the values for which $\chi^2 = (1 + \Delta/65)\chi_{min}^2$ where $\Delta = 0.25, 4.0$, or 4.61 . The outer contour corresponds to the formal 90% confidence limit for two interesting parameters. For each value of the inclination, the mass of the companion corresponds to within a small uncertainty. The long-dash curve represents the radius of the Roche lobe of the companion star, the medium-dash curve represents the radii where grazing eclipses would occur, and the three short-dash curves represent the radii of stars on the zero-age main sequence (ZAMS), stars that have exhausted half of the hydrogen at their centers, and stars on the the terminal age main sequence (TAMS; see text). The mass-radius relations were provided by Podsiadlowski (2004, private communication).

file that is consistent with the column density measurements yields a wind mass flux if we assume a wind terminal velocity. We use the prescription given in Vink, de Koter, & Lamers (2000), which predicts wind terminal velocities on the basis of the stellar mass, stellar radius, effective temperature, and luminosity (see also Lamers, Snow, & Lindholm 1995). In turn, we interpolate the stellar evolution calculations of Podsiadlowski for main sequence stars to estimate effective temperatures. Thus, we have not carried out this calculation for stellar radii smaller than those on the zero-age main sequence or larger than those on the terminal-age main sequence (see Fig. 11). We can compare these “observed” wind mass fluxes with those expected for a star with given mass, effective temperature, and luminosity. The “expected” mass flux is computed using formulae also presented by Vink et al. These formulae are based on empirical fits of mass fluxes inferred from ultraviolet, radio, and H α observations of many O and B stars. The same wind terminal velocity which we use to obtain an estimate of the

observed mass flux is used in the Vink et al. prescription for wind mass flux. The mass fluxes used by Vink et al. in the empirical fits are for single stars, and are not, in particular, for stars in binaries which nearly fill their Roche lobes.

We find that the “observed” wind mass loss rate is larger in all cases than the “expected” mass loss rate. In Fig. 11, medium-size dots show those combinations of system parameters in which the “observed” wind mass loss rate exceeds the “expected” rate by a factor of 3 or less. In the other cases for which we computed the “observed” wind mass loss rate, it exceeds the “expected” rate by more than a factor of 3, and often by more than a factor of 10. Most of these dots apply only to the $\beta = 1$ case; one dot applies to the $\beta = 1/2$ case; none apply to the $\beta = 0$ case.

The “expected” mass flux most closely approaches the “observed” mass flux for the case with $\beta = 1$, $M_c = 22.8M_\odot$, $R_c = 20.0R_\odot$, $v_\infty \sim 800 \text{ km s}^{-1}$ for which we obtain $\dot{M}_{\text{obs}} \sim 2.1 \times 10^{-6} M_\odot \text{ yr}^{-1}$ and $\dot{M}_{\text{exp}} \sim 1.5 \times$

TABLE 4
SYSTEM PARAMETERS

Parameter	$\beta = 0$	$\beta = 1/2$	$\beta = 1$
i	$54^\circ - 72^\circ$	$43^\circ - 70^\circ$	$38^\circ - 68^\circ$
a (lt-s)	58 - 65	58 - 75	59 - 81
M_c (M_\odot)	9 - 14	9 - 22	10 - 31
R_c (R_\odot)	4 - 15	4 - 19	4 - 22
$N_{H_{\text{wind}}}(\phi = 0)^a$ (10^{22} cm^{-2})	3.4 - 6.8	3.1 - 6.9	2.5 - 6.8
\dot{M} ($10^{-6} M_\odot \text{ yr}^{-1}$)	2.3 - 15	1.9 - 15	1.3 - 14

NOTE. — Each parameter range is defined by $\chi^2 < (1 + 4.61/65)\chi_{\text{min}}^2$ for the fits of eq. 7 to the measured column densities. The parameter ranges are also restricted by the requirements that $R_c \leq R_{\text{eclipse}}$, $R_c \leq R_{\text{Roche}}$, and by $R_{\text{ZAMS}} \leq R_c \leq R_{\text{TAMS}}$ for the associated value of M_c , i.e., the radius of the companion star is required to be in the range of radii of the main sequence stars calculated by Podsiadlowski (see Figs. 10 and 11).

^aThe column density of the wind in the radial direction outward to infinity from the position of the neutron star.

$10^{-6} M_\odot \text{ yr}^{-1}$. Note that this case is not realistic because the companion radius is equal to the radius of its Roche lobe. It is likely that the companion underfills its Roche lobe; otherwise the mass accretion rate would be higher and the X-ray luminosity would be expected to be at the Eddington limit.

6. DISCUSSION

We have found 605 s pulsations in the X-ray intensity of X1908+075. Doppler shifts of the pulse frequency, and changes in the intensity and low-energy attenuation that cyclically recur at the previously known orbital period of 4.4 days allow us to measure orbital parameters and to conclude that the system contains a highly magnetized neutron star orbiting in the wind of a massive companion star.

The observed variations in the shape of the spectrum and in the overall intensity indicate that the X radiation from the neutron star is both absorbed and scattered in the wind. We have estimated the absorption on the basis of a crude spectral model that assumes that any attenuation is caused by photoelectric absorption in neutral (unionized) gas with solar element abundances. In this model, we did not include the effects of the photoionization of the wind by the X-rays. We can now use our estimates of the wind column density and the X-ray luminosity to roughly estimate the ionization parameter $\xi = L_X / nr^2$ (Tarter, Tucker, & Salpeter 1969) at a typical location in the binary system, where n is the number density of atoms in the wind and r is the distance from the X-ray source. If we take the orbital radius a as a characteristic distance within the binary system, i.e., we set $r = a$, and for a density use $n \sim N_{H_{\text{wind}}}(\phi = 0)/a$, we obtain $\xi = L_X / (N_H a) \sim 20\text{--}60 \text{ ergs cm s}^{-1}$. Under these conditions we would expect that most atoms would lose their outer electrons, but atoms of carbon, oxygen, etc. would retain at least their K-shell electrons (Tarter et al. 1969; Kallman & McCray 1982). Krolik & Kallman (1984) have estimated the equilibrium conditions of gases photoionized by continuum X-ray spectra. They consider the condition of the gas as a function of a modified ionization parameter $\Xi = L_X / (4\pi c n r^2 kT)$ where c is the speed of light, k

is Boltzmann's constant and T is the gas temperature. For a characteristic location in the X1908+075 system, we have $\Xi \sim 8(T/10^5 \text{ K})^{-1}$. For each of the two spectral shapes that Krolik & Kallman (1984) consider in detail, one can roughly sketch the parameters of a self-consistent solution taking into account that the actual density will be higher than that estimated on the basis of the neutral matter absorption cross section. The parameters of the solutions in the two cases are roughly the same: $T \sim 4 \times 10^4 \text{ K}$, $\Xi \sim 10$, the X-ray opacity in the $\sim 2\text{--}6 \text{ keV}$ band is reduced by a factor of ~ 2 from the value expected for cold neutral gas of cosmic abundances, and $N_{H_{\text{wind}}}(\phi = 0) \sim 1 \times 10^{23} \text{ cm}^{-2}$. Since, in this regime, the temperature is a steep function of Ξ , it is likely to vary over a wide range at different places in the system. A more realistic estimate of the physical properties of the wind would need to self-consistently consider the actual source X-ray spectrum, the wind velocity, the possibility of non-solar abundances, the position-dependent degree of ionization in the wind, the effects of the ionization upon the wind acceleration, and the transfer of radiation in the system including both the effects of scattering and absorption. This is beyond the scope of this paper.

Using our fitted column densities and wind speeds estimated from the formula of Vink, de Koter, & Lamers (2000), we find the mass loss rate in the wind from the companion star to be $\gtrsim 1.3 \times 10^{-6} M_\odot \text{ yr}^{-1}$ for all the cases with acceptable values of χ^2 and with companion star radii in the range expected for main sequence stars. For those cases where the estimated mass loss rate is not more than a factor of order 3 greater than an empirical prediction based on the stellar mass, temperature, and luminosity, we find the rate must be $\gtrsim 2 \times 10^{-6} M_\odot \text{ yr}^{-1}$. The depression of the X-ray opacity of the gas from ionization implies that the wind mass loss rate must be higher than this latter rate, likely, as discussed above, by a factor of two and possibly by a larger factor.

As noted in §5, over the allowed region of the $M_c - R_c$ plane that we have identified, such mass loss rates are significantly higher than those predicted using the empirically-based mass loss rate prescriptions of Vink et al. However, one should note that these prescriptions do not take into account any of the effects of the star being in a binary system, including the presence of a critical potential lobe. Furthermore, we used the effective temperatures computed by Podsiadlowski for stars that evolve without mass loss and without being affected by any of the phenomena that occur in a binary system. Thus, we cannot exclude the possibility that the companion star is on the main sequence.

Another possibility is that the companion is a Wolf-Rayet (WR) star. A WR star could well have a mass that is consistent with the value that we find for the companion, but its radius would be much smaller than that of a main-sequence star of comparable mass. It would have a prodigious wind (Nugis & Lamers 2000) that could reach or surpass the mass loss rate that we infer (with assumptions) for X1908+075. According to Nugis & Lamers (2000), WR stars of either type WN or WC and mass in the range $\sim 9\text{--}15 M_\odot$ have wind mass loss rates between 4 and $20 \times 10^{-6} M_\odot \text{ yr}^{-1}$. Of course, the winds of WR stars, which have little or no hydrogen, would have significantly larger X-ray absorption cross sections per unit mass than winds from unevolved

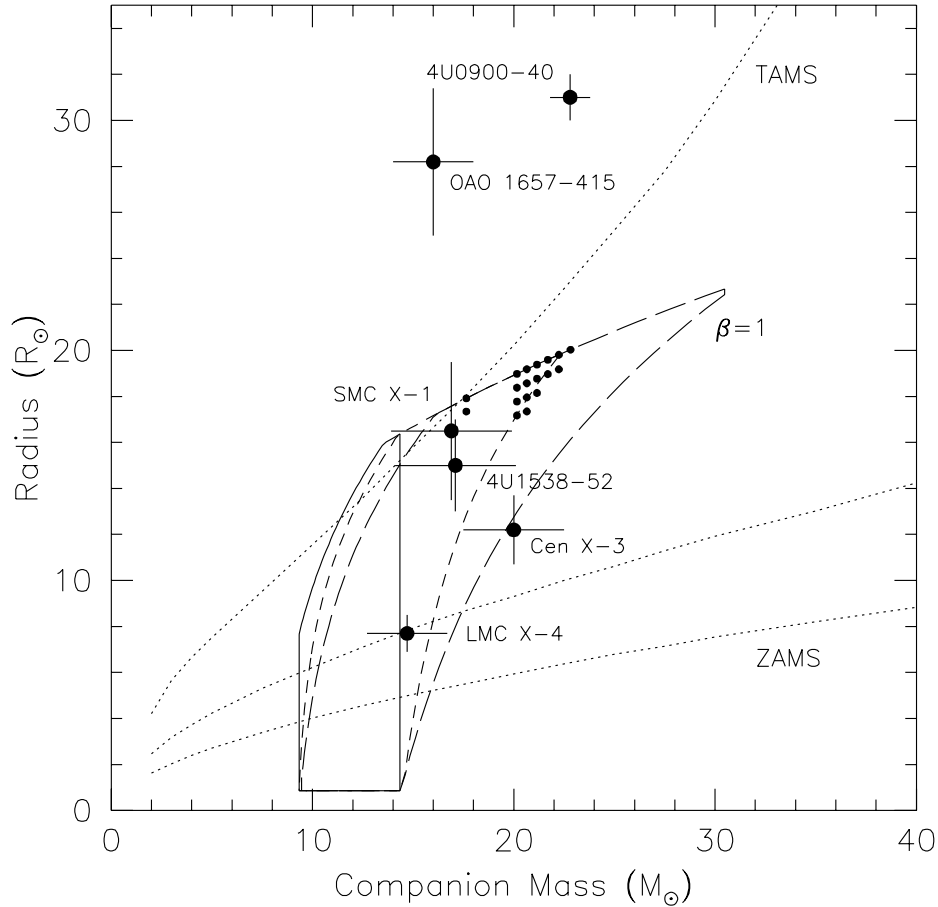


FIG. 11.— Limits on the companion star radius as a function of the companion mass determined from fits of the variation of column density with orbital phase. The solid, short-dashed, and long-dashed lines show limits from the $\beta=0$, $1/2$, and 1 fits, respectively, and correspond to the formal 90% confidence contours (cf. Fig. 10). High values of M_c correspond to low values of i and vice versa. The lower bounds on the radius are arbitrarily set at $\sim 1 R_\odot$. The medium-size dots show those fits for which the wind mass loss rate inferred from the observations is no more than a factor of 3 greater than the rate predicted by the recipe in Vink, de Koter, & Lamers (2000), (see text). The dotted curves are mass-radius relations for main-sequence stars where the mass is that indicated on the horizontal axis; the lowest curve represents the zero-age main sequence, the middle curve represents stars that have exhausted half of the hydrogen at their centers, and the upper curve represents the terminal age main sequence (see text). The mass-radius relations were provided by Podsiadlowski (2004, private communication). Also shown on the plot are the measured masses and radii of the “normal” stars in six well known high-mass X-ray binaries (Joss & Rappaport 1984; Nagase 1989; A. Levine 1984, private communication). The associated error bars crudely represent 90% confidence uncertainties.

stars. If there is little hydrogen in the wind, we may have *overestimated* the wind mass loss rate, but such a composition would nonetheless clearly indicate the WR nature of the companion.

If the companion star is indeed a WR star, then the X1908+075 system has potentially important implications, in general, for binary stellar evolution, and for the formation, in particular, of neutron star–black hole (NS-BH) systems. If it is a WR star, then it is likely the He or CO remnant core of a star that was originally much more massive, possibly of mass $\sim 23\text{--}35 M_\odot$ (e.g., Hurley, Pols, & Tout 2000). In this case we expect the companion to undergo core collapse in 10^4 to 10^5 years and leave behind a stellar-mass black hole (Brown et al. 2001). Thus, there is a possibility that the X1908+075 system is the progenitor of a neutron star–black hole binary where the neutron star formed first. This would be significant in at least two ways. First, in spite of

the fact that six NS-NS binaries have been discovered (see, e.g., Burgay et al. 2003; Champion et al. 2004), no NS-BH binaries have yet been found. There are theoretical arguments (Sipior, Portegies Zwart & Nelemans 2004; Pfahl, Podsiadlowski, & Rappaport 2004) which suggest that the latter binaries should be at least a factor of 10 less populous than their NS-NS cousins (but see Voss & Tauris 2003). An identified progenitor would help theorists better estimate the current population of NS-BH binaries. Second, if NS-BH binaries are formed, the issue of which collapsed star forms first is also important to our understanding of binary stellar evolution. The most direct way of producing these systems is for the BH to form first (from the more massive component of the system; see, e.g., Portegies Zwart, Verbunt, & Ergma 1997; Brown et al. 2000; Fryer & Kalogera 2001; Nelemans & van den Heuvel

2001; Lee, Brown, & Wijers 2002; Podsiadlowski, Rappaport, & Han 2002), but there are also channels where the NS forms first, as discussed above (see, e.g., Voss & Tauris 2003).

Since this paper was originally written, Morel & Grosdidier (2004) have reported the results of near-infrared observations of stars in or close to the error box of X1908+075, and have found a star whose JHK magnitudes and colors, and H and K band spectra, suggest an O or B supergiant at $d \sim 7$ kpc. They believe that this star is likely to be the counterpart of X1908+075. If confirmed, this identification would rule against a WR companion star. We expect to obtain

observations of X1908+075 with the Chandra X-ray Observatory, and to thereby obtain an X-ray position sufficiently accurate to secure the optical identification.

We thank Edward Morgan for assistance with the data preparation. We are grateful to Ph. Podsiadlowski for providing us with mass-radius relations for stars on the ZAMS and TAMS and for numerous helpful discussions. We are also grateful to Henny Lamers for giving us useful advice on stellar winds, and to an anonymous referee for helpful comments. One of us (SR) acknowledges support from NASA ATP Grant NAG5-12522.

REFERENCES

- Bildsten, L., Chakrabarty, D., Chiu, J., Finger, M. H., Koh, D., Nelson, R. W., Prince, T. A., Rubin, B. C. et al. 1997, *ApJS*, 113, 367
- Brown, G.E., Heger, A., Langer, N., Lee, C.-H., Wellstein, S., & Bethe, H.A. 2001, *New Astr.*, 6, 457
- Brown, G. E., Lee, C.-H., Wijers, R. A. M. J., & Bethe, H. A. 2000, *Phys. Rep.*, 333, 471
- Burgay, M., et al. 2003, *Nature*, 426, 531
- Castor, J. I., Abbott, D. C., & Klein, R. I. 1975, *ApJ*, 195, 157
- Champion, D. J., Lorimer, D. R., McLaughlin, M. A., Cordes, J. M., Arzoumanian, Z., Weisberg, J. M., & Taylor, J. H. 2004, *MNRAS*, 350, L61 [astro-ph/0403553]
- Delgado-Martí, H., Levine, A. M., Pfahl, E., & Rappaport, S. A. 2001, *ApJ*, 546, 455
- Fryer, C.L., & Kalogera, V. 2001, *ApJ*, 554, 548
- Groenewegen, M. A. T. & Lamers, H. J. G. L. M. 1989, *A&AS*, 79, 359
- Hurley, J.R., Pols, O.R., & Tout, C.A. 2000, *MNRAS*, 315, 543
- Jahoda, K., Swank, J. H., Giles, A. B., Stark, M. J., Strohmayer, T., Zhang, W., & Morgan, E. H. 1996, *Proc. SPIE*, 2808, 59
- Joss, P. C. & Rappaport, S. A. 1984, *ARA&A*, 22, 537
- Kallman, T.R., & McCray, R. 1982, *ApJS*, 50, 263
- Krolik, J.H., & Kallman, T.R. 1984, *ApJ*, 286, 366
- Lamers, H. J. G. L. M. & Cassinelli, J. P. 1999, *Introduction to stellar winds / Henny J.G.L.M. Lamers and Joseph P. Cassinelli*. Cambridge ; New York : Cambridge University Press, 1999. ISBN 0521593980
- Lamers, H.J.G.L.M., Snow, T.P., & Lindholm, D.M. 1995, *ApJ*, 455, 269
- Lee, C., Brown, G., & Wijers, R. 2002, *ApJ*, 575, 996
- Lucy, L. B. & Solomon, P. M. 1970, *ApJ*, 159, 879
- Morel, T. & Grosdidier, Y. 2004, *MNRAS*, submitted
- Nagase, F. 1989, *PASJ*, 41, 1
- Nelemans, G., & van den Heuvel, E.P.J. 2001, *A&A*, 376, 950
- Nugis, T., & Lamers, H.J.G.L.M. 2000, *A&A*, 360, 227
- Pfahl, E., Podsiadlowski, Ph., & Rappaport, S. 2004, in preparation
- Podsiadlowski, Ph., Rappaport, S., & Han, Z. 2002, *MNRAS*, 341, 385
- Sipior, M. S., Portegies Zwart, S., & Nelemans, G., astro-ph/0407268
- Portegies Zwart, S.F., Verbunt, F., & Ergma, E. 1997, *A&A*, 321, 207
- Puls, J., et al. 1996, *A&A*, 305, 171
- Rothschild, R. E., et al. 1998, *ApJ*, 496, 538
- Shull, J. M. & van Steenberg, M. E. 1985, *ApJ*, 294, 599
- Sobczak, G. J., McClintock, J. E., Remillard, R. A., Cui, W., Levine, A. M., Morgan, E. H., Orosz, J. A., & Bailyn, C. D. 2000, *ApJ*, 544, 993
- Tarter, C.B., Tucker, W.H., & Salpeter, E. E. 1969, *ApJ*, 156, 943
- Vink, J.S., de Koter, A., & Lamers, H.J.G.L.M. 2000, *A&A*, 362, 295
- Voss, R., & Tauris, T.M. 2003, *MNRAS*, 342, 1169
- Wen, L., Remillard, R.A., & Bradt, H.V. 2001, *ApJ*, 532, 1119